

Wave Energy Flux Variability in the Caribbean Sea

Andrés Fernando Orejarena

INVEMAR

Juan Manuel Sayol

Universidad de Alicante - Campus San Vicente del Raspeig: Universitat d'Alacant

Ismael Hernández-carrasco

ICTS SOCIB: Sistema d'observacio i prediccio costaner de les Illes Balear

Alejandro Cáceres

Universite de Toulon

Juan Camilo Restrepo

Universidad del Norte

Alejandro Orfila (✉ a.orfila@uib.es)

CSIC: Consejo Superior de Investigaciones Cientificas <https://orcid.org/0000-0002-1016-8726>

Research Article

Keywords: Wave energy flux, Spatio-temporal variability, Caribbean Sea, Self Organized Maps, El Niño-Southern Oscillation

Posted Date: January 10th, 2022

DOI: <https://doi.org/10.21203/rs.3.rs-1229355/v1>

License: © ⓘ This work is licensed under a Creative Commons Attribution 4.0 International License.

[Read Full License](#)

Wave energy flux variability in the Caribbean sea

Andrés F. Orejarena-Rondón · Juan-Manuel
Sayol · Ismael Hernández-Carrasco ·
Alejandro Cáceres-Euse · Juan C.
Restrepo · Alejandro Orfila

Received: date / Accepted: date

Abstract Wave energy flux (WEF) is assessed in the Caribbean Sea from a 60-year (1958–2017) wave hindcast. We use a novel approach, based on neural networks, to identify coherent regions of similar WEF and their association with different climate patterns. This method allows for a better evaluation of the underlying dynamics behind seasonal and inter-annual WEF variability, including the effect induced by the latitudinal migration of the Intertropical Convergence Zone (ITCZ), and the influence of El Niño-Southern Oscillation events. Results show clear regional differences of the WEF variability likely due to both a clear regionalization of the WEF due to both the intensification and migration of the ITCZ. WEF exhibits a strong semiseasonal signal in areas of the continental shelf, with maximums in January and June, in agreement with the sea surface temperature and sea level pressure variability. At larger scales, WEF shows a significant correlation with the Oceanic Niño Index depicting positive values in the central and western basin and negative ones at the eastern side.

A. Orejarena-Rondón
Program of Marine and Coastal Geosciences, INVEMAR, Santa Marta, Colombia

J.M. Sayol
Department of Applied Mathematics, University of Alicante, 03690 Sant Vicent del Raspeig,
Alicante, Spain
E-mail: juanma.sayol@ua.es

I. Hernández-Carrasco
Sistema de Observación Costero de les Illes Balears, SOCIB, 07007 Palma de Mallorca, Spain
Mediterranean Institute for Advanced Studies, IMEDEA (CSIC-UIB), 07190 Esporles, Spain

A. Cáceres-Euse
Mediterranean Institute of Oceanography, MIO, Université de Toulon, 83041 Toulon, France

J. C. Restrepo
Dpto. de Física y Geociencias, Universidad del Norte, Puerto Colombia, 081007, Colombia

A. Orfila
Mediterranean Institute for Advanced Studies, IMEDEA (CSIC-UIB), 07190 Esporles, Spain
Tel.: (+34)971611239
E-mail: alejandro.orfila@csic.es

Keywords Wave energy flux · Spatio-temporal variability · Caribbean Sea · Self Organized Maps · El Niño-Southern Oscillation

1 Introduction

The wave energy flux (WEF) provides information on the magnitude and temporal variations of the energy transferred from the atmosphere to the ocean over selected periods of time (e.g. months, seasons or even years) [Dodet et al., 2010, Ardhuin and Orfila, 2018]. It also extracts key details on sea surface waves that may not be detected from single parameters, such as significant wave height (H_s) or wave period (T_{m-01}), becoming a more suitable indicator to capture wave climate variations [Reguero et al., 2019]. Long time series of WEF can be used to determine potential impacts on coastal zones, such as variations in the planform of beaches allowing to assess eventual impacts of future wave variations on coastal areas [Fiedler et al., 2015, Elshinnawy et al., 2017]. Additionally, ocean waves is one of the renewable energy resources that has attracted more attention in the last years due to its potential capability of providing green and sustainable electricity offering several advantages with respect to other energy resources [Lin et al., 2019, Arinaga and Cheung, 2012, Liang et al., 2017]. Therefore a precise characterization of the spatial and temporal variability of WEF is crucial to evaluate the local and regional impact of the evolving wave climate in the context of the ongoing global warming [Wiggins et al., 2019, Elshinnawy et al., 2017, Hanson et al., 2003]. However, due to the scarcity of wave measurements around the world, to get the spatio temporal distribution of WEF we need to use validated wave hindcasts provided by numerical models [Mentaschi et al., 2017, Mirzaei et al., 2015, Waters et al., 2009, Iglesias et al., 2009].

Previous studies have analyzed inter-annual and long-term WEF variations associated with climate indices (e.g. El Niño-Southern Oscillation (ENSO), Pacific Decadal Oscillation (PDO), Tropical North Atlantic index (TNA)) and climate change projections, respectively. On a global scale, [Reguero et al., 2019] found from a 60-year wave reanalysis that wave power has increased at a rate of 0.4% per year at global scale. These results indicate that the anthropogenic global warming is strengthening synoptic winds in some regions, thus favoring the generation of larger surface waves and affecting the global wave climate. [Reguero et al., 2015] characterized the mean wave power globally as well as its seasonal variability with a global wave reanalysis performed with WaveWatch3 model. Their results showed that the effect of the inter-annual variability is more prominent over the Northern Hemisphere, where the contribution of the seasonal variability is larger. [Wu et al., 2017] used ERA-Interim wave reanalysis data for the period 1997–2010 to evaluate WEF trends at global scale, as well as of time series of single parameters such as the significant wave height (H_s), mean wave period (T_{m-01}), and wave direction (θ_m). Among the studied parameters, they found a significant increase in the magnitude of WEF, H_s and T_{m-01} in southern mid-latitudes and in the western part of the North Atlantic and of the North Pacific. In contrast, they found a significant decrease of the same parameters in the eastern part of the tropical North Pacific [Wu et al., 2017]. [Mentaschi et al., 2017] analyzed global trends of extreme WEF along global coastlines during the 21st century under a high emission scenario (RCP 8.5). Results for this pessimistic projection would

imply an increase of WEF up to 30% for most of the southern mid-latitudes, while in the Northern Hemisphere many coastal areas displayed negative trends. They also showed that significant long-term trends in the extreme WEF are related with the intensification of inter-annual signals such as ENSO and the North Atlantic Oscillation (NAO). On regional and local scales, several dedicated model-based studies have been developed to evaluate the wave energy resource, either the spatial distribution or the temporal variability [Liberti et al., 2013, Ponce de León et al., 2016, Liang et al., 2017, Canals Silander and García Moreno, 2019, Cuttler et al., 2020, Guillou et al., 2020], which has helped to improve the design and deployment of wave energy converters in the study areas.

Previous studies have already characterized the wave power in the Caribbean sea. [Ortega et al., 2013] identified the best sites for a wave farm near the small island of Isla Fuerte by means of numerical simulations. [Osorio et al., 2015], assessed the wave power potential in the Colombian Caribbean showing that the highest values of mean wave power are of 5–7 kW/m from December to April. This potential is relatively small compared to other places around the world, where powers of about 40 kW/m and above are considered profitable to implement wave farms. [Appendini et al., 2015] studied the wave energy potential in the whole Caribbean Sea from a 30-year wave reanalysis detecting that below the influence area of the Caribbean Low Level Jet (CLLJ), in the central Caribbean, the amount of wave power presents values between 8 – 14 kW/m. They also mentioned the existence of large spatial wave power gradients, which need to be considered for the installation of energy extraction devices. [Guillou, 2020, Guillou et al., 2020] recently analyzed the wave energy and wave power resources for the whole North Atlantic, including the Caribbean Sea, using wave buoys at the open sea and a 30-year reanalysis, respectively. Several metrics were compared to quantify the useful wave energy, as well as its seasonal variability. The maximum WEF was found during late fall (December and January) and late spring (June and July) with wave power ranges in the Caribbean Sea within the range of previous studies (5 – 14 kW/m). Recently, [Orejarena-Rondón et al., 2022] used the same simulation we use in this work to analyze WEF trends in the Caribbean Sea, showing a decrease between 1958–2017 with an annual rate that oscillates between 0.01% and 0.2%, depending on the region. Here we go one step further to analyze the spatial and temporal variability of WEF in the Caribbean Sea from 1958 to 2017 using a novel approach with which coherent regions that show similar WEF are distinguished according to their associated wind pattern. By applying this method we get new insights on the physical processes that drive seasonal and inter-annual WEF changes, including the impact of ITCZ migration and ENSO events.

The article is structured as follows: the main Caribbean Sea features are described in section 2. Data set and methods are outlined in section 3. Section 4 shows the main results including model validation, regional characterization of WEF and surface wind, as well as their temporal variability at seasonal and inter-annual scales. Finally, in section 5 we discuss the main results in the context of the current literature and the main conclusions are summarized.

2 Study area

The Caribbean Sea is located between latitudes $8.1^{\circ}\text{N} - 13.6^{\circ}\text{N}$ and longitudes $84.52^{\circ}\text{W} - 59.7^{\circ}\text{W}$, being bordered by the Lesser Antilles at the east, the Greater Antilles at the north, the eastern portion of Central America at the west and the northern coasts of South America at the south (Figure 1). Wave dynamics is mainly controlled by the westward surface trade winds, which show a large seasonality, and a low-level wind core with higher speeds that gives origin to the Caribbean Low Level Jet (CLLJ). The CLLJ has its kernel at a height of around 925 hPa, although can reach heights over 800 hPa and is located in the center of the basin [Amador, 1998, Poveda and Mesa, 1999, Poveda et al., 2006, Chunzai, 2007, Orfila et al., 2021]. Wind seasonality is associated to the meridional migration of the ITCZ, which is also responsible for the path and penetration of transient features as cold fronts and tropical storms [Poveda et al., 2006, Poveda, 2004, Andrade and Barton, 2013]. The meridional oscillation of the ITCZ responds to the seasonal insolation cycle. During the austral summer the ITCZ is located between Colombia and Ecuador, whereas it shifts northward in the boreal summer. When the ITCZ is located between $0 - 5^{\circ}\text{S}$, the northern trade winds dominate in these regions with an average speed that varies between 8 and 15 m/s [Andrade, 1993]. This seasonality is modulated by regional sea surface temperature and sea level gradients which add a semi-seasonal component [Chunzai, 2007].

Regarding atmospheric instability conditions, there is little rainfall from December to April over the Colombian basin and in the west of the Antilles. Conversely, in the Caribbean coasts surrounding the Gulf of Darien (which includes coasts of Colombia, Panamá and Costa Rica), it rains throughout almost the whole year [Andrade et al., 2013]. By contrast, when the ITCZ is located at a latitude between $10 - 12^{\circ}\text{N}$, from August to November, the weaker southern trade winds (with a mean speed ~ 4 m/s) reach the Colombian basin, contributing to the formation and even strengthening of tropical convective storms that may reach hurricane category over the western Caribbean Sea [Andrade et al., 2013]. As a result, the precipitation caused by the displacement of the ITCZ only affects the Colombian basin below 10°N . Consequently, trade winds (and hence the CLLJ) permanently remain above La Guajira peninsula. The rest of the year there is a transition period between the aforementioned seasons, in which trade winds weaken and some rainfall comes over the Colombia basin from April to June), while from June to August trade winds strengthen and rainfall decreases. The latter transition time is locally known as “Veranillo de San Juan” from its name in Spanish [Poveda et al., 2006, Andrade et al., 2013].

Winds and rainfall are sensitive to the arrival of oscillations such as easterly waves, with periods of 7 days, and cold fronts, coming from North America and crossing the Caribbean towards the East in about 10 to 14 days generating precipitation and rising wind stress on its way [Andrade et al., 2013, Alvarez-León et al., 1995]. Large-scale signals such as the Madden-Julian Oscillation have longer periods (40 to 50 days) and have been detected in sea surface temperature and in rainfall records in Santa Marta, Colombia, at a latitude above 11°N [Rivera-Páez and Molares, 2003, Andrade et al., 2013]. Moreover, there is also a strong inter-annual variability associated with ENSO that affects both Atlantic and Caribbean coastal areas. [Huang et al., 2002, Enfield and Mayer, 1997] determined that at the end of the year, when El Niño events tend to become stronger, trade winds weaken

over the eastern Caribbean Sea at a latitude between 10°N and 20°N , extending until Africa. In contrast, in the western part of the Caribbean Sea trade winds strengthen during El Niño events.

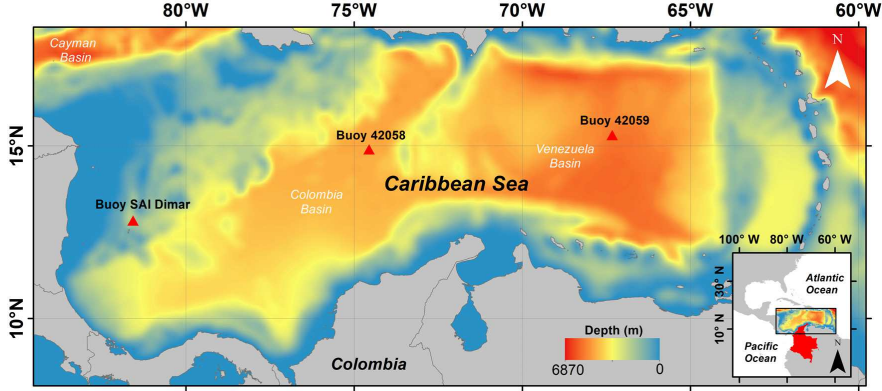


Fig. 1 SWAN domain used for the 60-year wave simulation in the Caribbean basin. Red triangles indicate the location of buoys used for the validation: Buoy SAI DIMAR, NOAA buoy 42058, and NOAA buoy 42059, ordered from west to east.

3 Data and Methods

3.1 Wind data

Surface wind fields used to force the The Simulating WAVes Nearshore (SWAN) model in the study area correspond to the JRA-55 simulation performed by the Japan Meteorological Agency. This data was the first complete reanalysis in covering the last half century (1958–2020), and the first one that applied a four dimensional variational analysis [Kobayashi et al., 2015]. This set of global atmospheric data is suitable to study multidecadal variability and the relation of wave climate with climate change [Japan Meteorological Agency, 2013]. Output fields provide the 10 m height wind speed (u_w, v_w) on a mesh of 23×43 grid points with a spatial resolution of $0.5625^{\circ} \times 0.5616^{\circ}$. The data cover the whole study area from 84.3746°W , 7.5819°N (lower left corner) to 60.1871°W , 19.9371°N (upper right corner) from 1958–2017 (both included) with a 3-hourly temporal resolution.

3.2 SWAN Model

The SWAN model solves the wave action balance equation for the propagation of the wave spectrum, which allows for realistic estimations of wave parameters in the open ocean and in coastal areas [Booij et al., 1999]. The SWAN domain covers an area of $2600 \text{ km} \times 1175 \text{ km}$ distributed into 229×101 grid cells (Figure 1). The bathymetry of the Caribbean Sea was obtained from Colombian Hydrographic Service nautical charts as well as from the general ocean bathymetric chart GEBCO.

Waves were simulated in non-stationary mode using the JRA-55 wind fields. Wind-induced wave growth was configured as exponential following the formulation of [Komen et al., 1984], while nonlinear deep water interactions were parameterized following the *Webb-Resio-Tracy* method. Other relevant processes, such as wave breaking, whitecapping energy dissipation, and bottom friction were included in the simulations. The integration time step was set as 30 minutes and H_s , T_{m-01} , and θ_m output data were recorded every 3 hours in each domain grid cell. H_s and T_{m-01} were validated through a comparison with in situ wave data measured by the NOAA-42058 buoy, which is located in the central Caribbean Sea (Figure2). The wave reanalysis we use in this work is published at [Orejarena-Rondón et al., 2021a].

3.3 Wave Energy Flux (WEF) calculation

Departing from the 3-hourly SWAN model output fields (H_s , T_{m-01} , θ_m), the monthly mean WEF was determined for the period 1958 – 2017. The WEF was computed as:

$$\overrightarrow{FE} = \frac{1}{64\pi} \rho g^2 T_{m-01} H_s^2 \frac{\overrightarrow{k}}{|\overrightarrow{k}|} \quad (1)$$

where ρ is the seawater density in kg/m^3 , g is the gravity acceleration, T_{m-01} is the mean period, H_s is the significant wave height and \overrightarrow{k} is the wavenumber vector. Departing from these components, we carried out a spatial and temporal characterization of the mean WEF in the Caribbean basin through a Self-Organizing Map analysis. Similarly, we have analyzed the inter-annual variability of the monthly mean WEF over time through a correlation analysis with ENSO indices.

3.4 Self-Organizing Map (SOM)

Self-Organizing Map is a statistical tool used to compress the information contained in a large amount of data into a single set of maps [Kohonen, 1982, Teuvo, 1997], reducing the high dimensional feature space of input data to a lower dimensional network of units called neurons. This unsupervised learning neural network is able to extract patterns from large data set mimicking the topological distribution of the neurons response in the brain. Learning processes are carried out by an interactive presentation of the input data to a preselected neuronal network, which is modified during the iterative process. Each unit is represented by a weight vector with a number of components equal to the dimension of the input data. During each iteration, the neuron whose weight vector is closest to the presented sample input data vector, called Best-Matching Unit (BMU), is updated together with its topological neighbors toward the input sample (see [Hernández-Carrasco and Orfila, 2018] for a more detailed description of the SOM process). When the probability density function of input data is approximated by SOM, and each unit is associated with that reference pattern that has a number of components equal to the number of variables in the data set, the training process finishes. Thus, this process can be interpreted as a generalization of similar observations.

In this study, a joint SOM analysis is applied over the monthly mean fields of both WEF and surface wind in the area covered by the 60-year wave reanalysis. In the case of the spatial analysis, since each iteration has associated a time and a location of the sample, we can obtain the evolution of a particular pattern computing the BMU for each sample. In the temporal domain the analysis of the neurons provide temporal patterns and the BMU is used to localize in space the temporal variability, providing regions of similar co-variability patterns.

3.5 Correlation and Cross Wavelet Transform Analysis

To explore the link between monthly mean WEF and ENSO at inter-annual scales we have proceeded as follows. First, we performed a direct correlation analysis between the Oceanic Niño Index (ONI) and the monthly mean WEF time series at every grid cell within the study area (Figure 12). Second, the cross wavelet transform (XWT) and wavelet coherence (WTC) analysis is applied between the ONI index and the time series associated to each of the 9 regions determined by SOM. The XWT between the temporal signals of the mean WEF and ONI reveal those regions where energy variance is more correlated giving also information about their phase relationship. The XWT of any two time series x_n and y_n is defined as $W^{XY}(s) = W^X(s)W^{Y*}(s)$, where $*$ denotes the complex conjugate. Furthermore, the cross wavelet power is defined as $|W^{XY}(s)|$ and the complex argument as $\arg(W^{XY}(s))$. The latter represents the relative local phase between x_n and y_n , which we will depict by arrows. The WTC spectrum highlights how large is the covariance of these signals, regardless of the high power display [Grinsted et al., 2004, Nalley et al., 2016, Restrepo et al., 2019]. The degree of coherence of XWT is given by the following coefficient:

$$R_n^2(s) = \frac{|S(s^{-1}W_n^{XY}(s))|^2}{S(s^{-1}|W_n^X(s)|^2) \cdot S(s^{-1}|W_n^Y(s)|^2)} \quad (2)$$

where S is a smoothing operator with values ranging between 0 (no correlation) and 1 (perfect correlation). The relationship between WEF and ONI is identified by the phase angle observed in the spectrum. An in phase relationship is indicated by the arrows pointing to the right. On the other hand, an out of phase relationship is indicated by arrows pointing to the left. Arrows that do not point straight to the right or to the left indicate a lagged correlation relationship.

4 Results

4.1 Wave model validation

Validation of SWAN simulation is performed with the NOAA buoy 42058, which is located in the central Caribbean Sea, using both H_s and T_{m-01} (see Figure 1). Conversely, due to the unavailability of other parameters, only modeled H_s can be validated with those buoys located near of San Andres Island: buoy SAI Dimar and NOAA buoy 42059, which are located at the west and east of the basin, respectively (see Figure 1). In the case of the buoy NOAA-42058, a good fit between *in-situ* and model data was obtained. For H_s , bias, correlation and

Willmot coefficients values of 0.064, 0.83, and 0.9 were obtained respectively, while for T_{m-01} , bias, correlation, and Willmot coefficients have values of 0.089, 0.74 and 0.77, respectively (Figure 2). For the other two buoys, a good fit was found between modeled H_s and *in-situ* H_s estimates. Correlation coefficients for buoy NOAA 42059 and buoy SAI Dimar were 0.7 and 0.91, respectively (Figure 3). Willmot coefficient values were 0.822 and 0.974 for buoy NOAA 42059 and buoy SAI Dimar, respectively, while bias coefficients for buoy NOAA 42059 and buoy SAI Dimar of 0.03 and 0.0034, respectively.

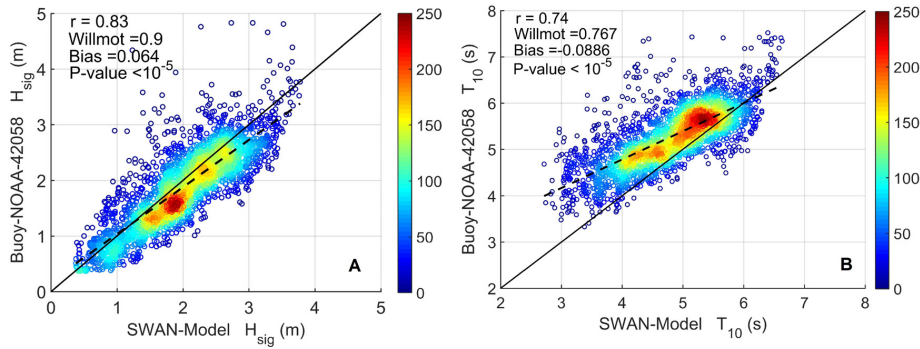


Fig. 2 Validation of: (A) significant wave height, H_s , and (B) wave period (T_{m-01}) in the central Caribbean Sea between SWAN simulation and observations provided by buoy 42058 (Figure 1). Color scale of dispersion diagrams corresponds to associated density of data used for validation. The linear regression is represented by a black dashed line.

4.2 Characterization of mean WEF and surface wind in the Caribbean Sea

Monthly mean and standard deviation of WEF and surface wind are shown in Figure (4 A - B and C - D, respectively). The large mean wind speed is reflected in the intensification of the Caribbean Low Level Jet (CLLJ) over approximately 68°W to 80°W and between 12°N and 16°N , with average speeds between 8 and 10 m/s . Wave response to this forcing is shown in Figure 4A, where WEF starts to rise dramatically at about 70°W and then extends toward the west of the basin. As the WEF is related with the wave height and the period, when the WEF reaches the highest values (1400 W/m , between 75°W and 78°W), wind waves are completely developed. The standard deviation of both mean wave energy flux and wind fields in the study area are shown in Figures 4B and D. The largest deviation for the mean WEF is obtained between 75°W - 80°W and 12°N - 16°N , whilst for wind speed this is obtained between 73°W - 80°W and 10°N - 13°N .

4.3 Spatial patterns of monthly mean WEF over the Caribbean Sea from SOM Analysis

As mentioned above, spatial patterns are obtained by applying a joint SOM analysis between the monthly mean WEF and the monthly mean horizontal wind fields.

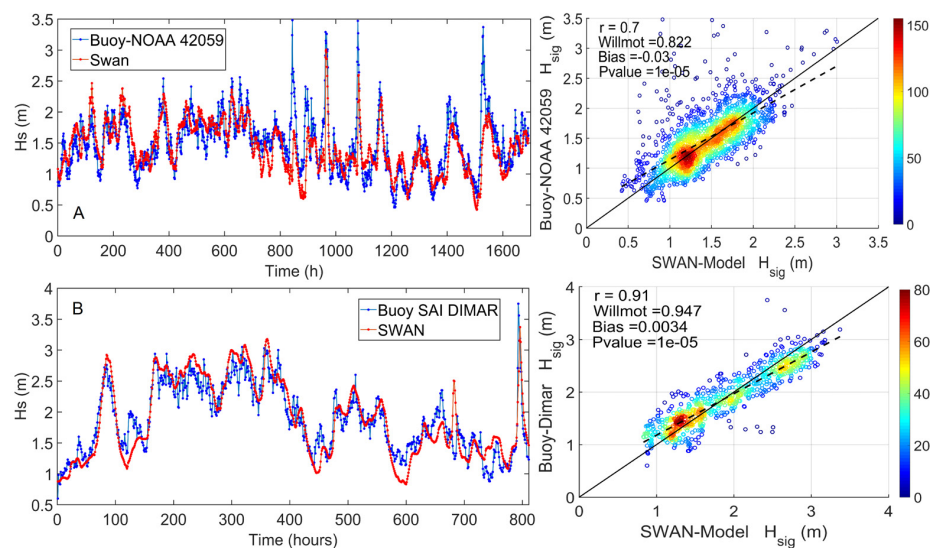


Fig. 3 Validation of H_s in the west and east of Caribbean basin (see buoys SAI DIMAR and NOAA 42059 in Figure 1, respectively). Color scale of dispersion diagrams corresponds to associated data density used in the validation. The linear regression is depicted by a black dashed line.

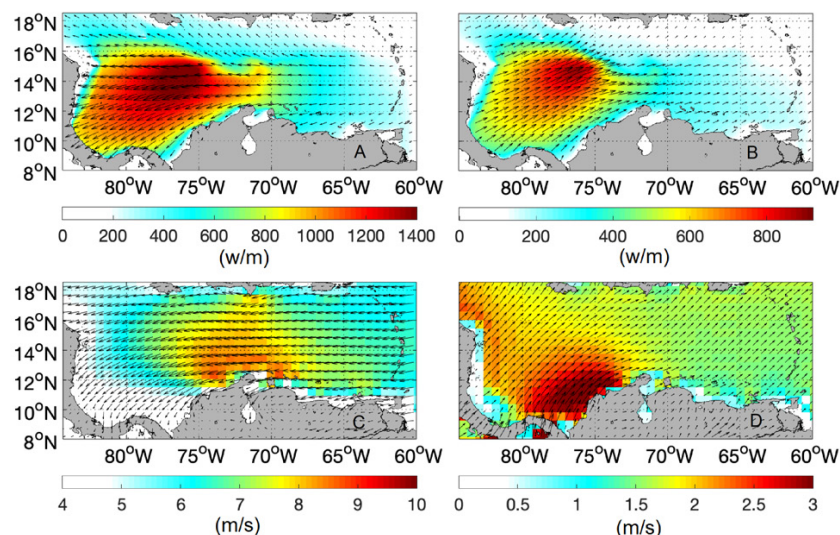


Fig. 4 (A)-(C) Mean wave energy flux (WEF) and wind field used in the simulations, respectively. (B)-(D) Standard deviation of both mean WEF and wind fields. Colormaps represent the magnitude of WEF (in W/m, top panels) and wind speed (in m/s, bottom panels), respectively; and the arrows their direction.

The analysis is restricted to the Caribbean Sea and covers the period between 1958 and 2017. Figure 5 (top panels) and Figure 6 (top panels), show the coupled patterns obtained from the 3×3 SOM neurons of WEF and surface winds with their

corresponding probability of occurrence, which indicates how often these specific patterns occur over the 60 yr. In Figure 5 (bottom panels) and Figure 6 (bottom panels) the corresponding anomalies are shown for every neuron. Moreover, Figure 7 shows the monthly frequency occurrence of patterns determined by the best matching unit (BMU). The BMU is obtained comparing all patterns (1–9) with each sample of the mean WEF to calculate the frequency of occurrence and select the pattern more similar to the sample.

All patterns shown in the top panel of Figures 5 and 6 are restricted to a common area in the western Caribbean Sea strongly influenced by the CLLJ. Patterns with the largest probability of occurrence (P1, P6 and P7), are associated with the meridional migration of the ITCZ throughout the year (Figure 7). P1, with an occurrence of 22.6%, is associated with the dry season (December to April, see Figure 7), with the highest probability occurring from January to March (> 35%). P7, with an occurrence of 14.6%, is associated with the transition season. This pattern is presented with a low frequency of occurrence during May and August, and with high frequency during June and July (> 35%), when the “Veranillo de San Juan” occurs. P6, with an occurrence of 10.4%, is associated with the wet season (from August to November). The highest frequency of occurrence of this pattern is presented during the months of September and October (> 35%). This pattern also appears in May, a month that corresponds to the transition period, but with lower frequency of occurrence (15%).

Although with less probability of occurrence, other patterns (P2, P3, P4, P5, P8 and P9) also take place in any of the three climatic seasons. For instance, P2 and P4, with 6.7% and 4.4% probability of occurrence, have a low probability of occurrence during the dry season (March, April, May and December). P5 and P8, with 2.6% and 7.9% probability of occurrence each one, are associated with the transition season. P9, with 10.4% probability of occurrence, is associated with the wet season (low frequency of occurrence during June and October and intermediate probability during May, August and September). P3, with 13.3% probability of occurrence, is presented randomly throughout the year (see Figure 7): the highest probability is presented in November (30%), the intermediate one in April and December (20%), and low one in February and March (10%).

In order to assess the spatial and temporal changes of both WEF and surface wind fields we have computed the standard deviation of every SOM pattern (Figure 5 for the WEF and Figure 6 for the wind). The patterns with the largest variability are P1, P6 and P9 for WEF and P1 and P9 for wind, being in all cases restricted to the western Caribbean basin. As observed, the increase in the magnitude of the WEF and wind speed, are the result of both the displacement of the ITCZ and the intensification of trade winds.

4.4 Temporal patterns of WEF over the Caribbean Sea from SOM analysis

To better explore the dominant direction of WEF, we have applied a temporal SOM analysis over zonal (F_x) and meridional (F_y) components monthly mean WEF. As we use 3×3 neurons again, this analysis also provides 9 zones of co-variability in the Caribbean Sea (Figure 8). Figure 9 shows time series of F_x and F_y components for every region in top and bottom panels, respectively. The sign (+/-) in the abscissas indicates the direction of each components: a negative value

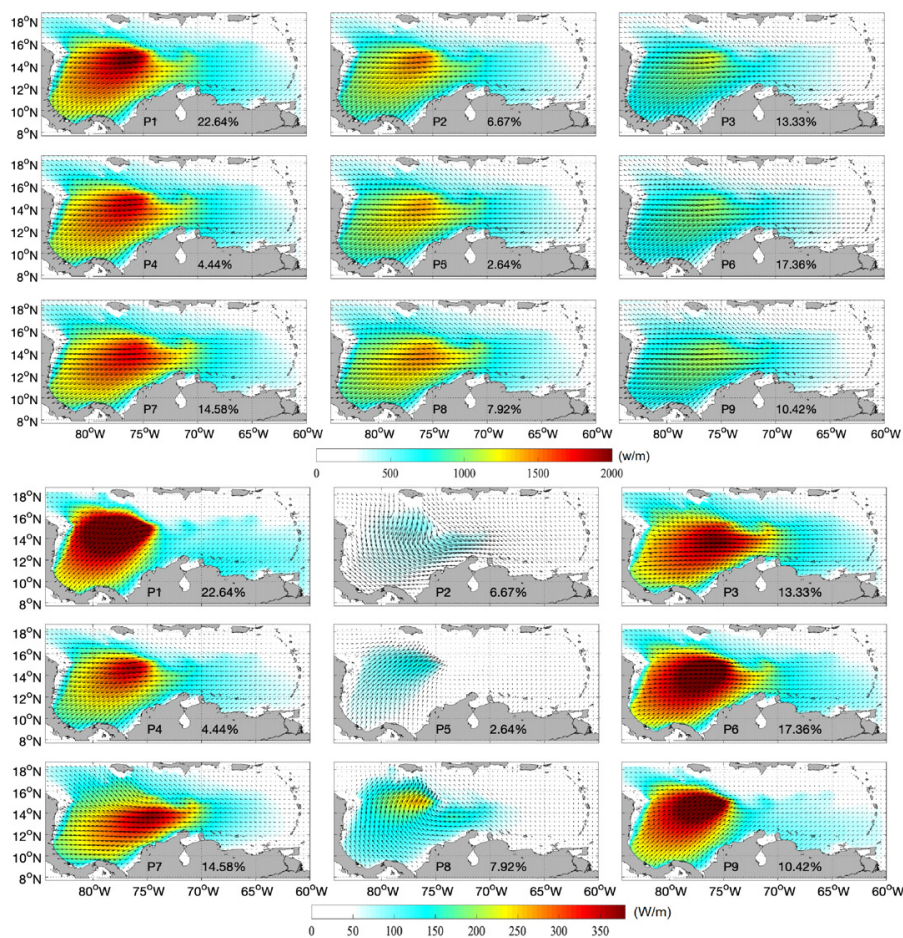


Fig. 5 Spatial patterns of mean wave energy flux (WEF) given by a 3×3 SOM analysis with their direction in the Caribbean basin (top panel). Standard deviation for the above mentioned spatial patterns (bottom panel). The percentage in each pattern reflects its total occurrence probability in %.

indicates a direction towards the west in the zonal component and towards the south in the meridional component, whereas a positive value indicates a direction towards the east in the zonal component and towards the north in the meridional one. Most of time series conserve the same sign, which allows to clearly identify the dominant direction.

As seen, the zonal component is generally two times larger than the meridional one. According to the magnitude of WEF we can distinguish three groups of zones: the largest values (in absolute magnitude) are observed in zones 7, 4, 1 (in decreasing order), located in the center and western areas of the Caribbean Basin, from 70°W , extending toward the south and to the west of the basin (Figure8). Time series of WEF associated with zone 7 (Tp7 in top and bottom panels) reach values between -1300 and -400 (W/m) for F_x , and between -220 and 0 (W/m) for F_y (Figure9), which indicates that WEF is predominantly oriented WSW-W over

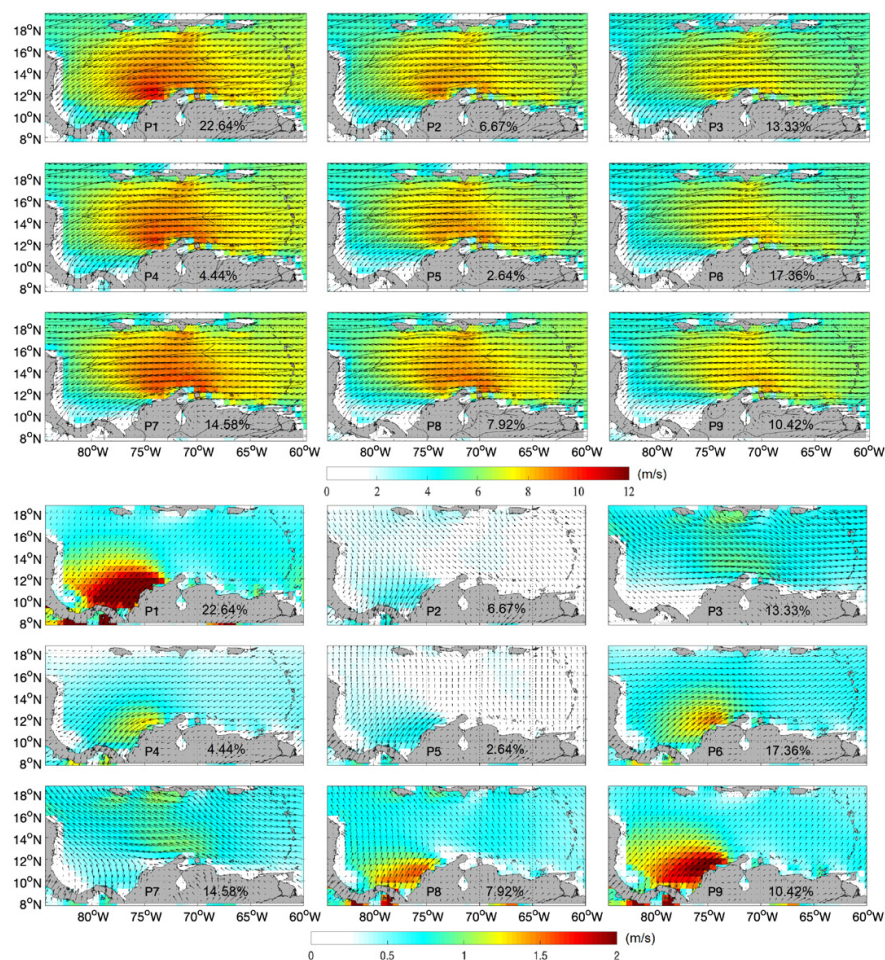


Fig. 6 Spatial patterns of wind fields obtained from the SOM analysis given by a 3×3 with their respective direction, in the Caribbean basin (top panel). Standard deviation for the computed above mentioned spatial patterns (bottom panel). The number at the bottom-right in each pattern corresponds with total occurrence probability in %.

the 60 years. Similar results are found in zone 4, but with a stronger meridional component. In contrast, zone 1 shows weaker components and slightly turned to the south (oriented SW-WSW).

Moderate values of WEF are observed in zones 8, 5 and 2. These regions cover the center Caribbean basin between 64°W and 70°W , and extend toward the zone 7 (Figure 8). In zone 8, time series of u and v components take values between -1000 and -350 (W/m), and between -60 and 100 (W/m), respectively (Figure9). It indicates that WEF is predominantly oriented toward the W. Similarly, components in zone 5 are also mainly oriented toward the W, with values between -850 and -300 (W/m) and between -100 and 40 (W/m) (Figure9). Components of zone 2 show weaker zonal values, between -700 and -250 (W/m), and a stronger merid-

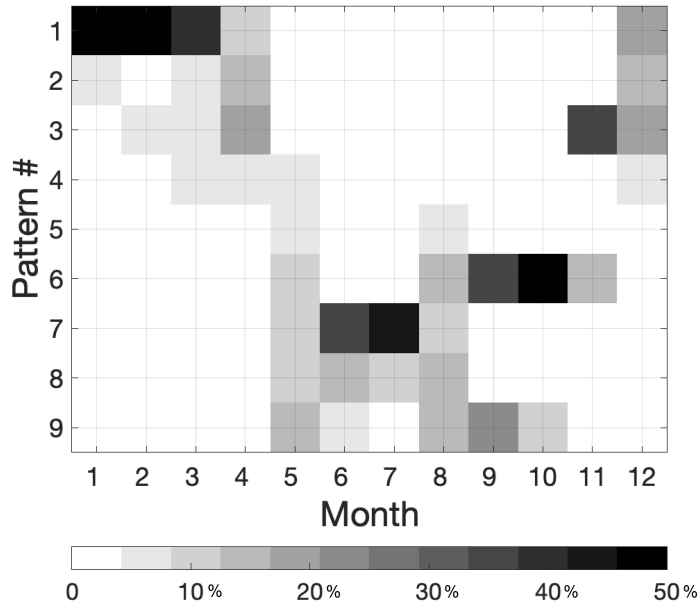


Fig. 7 Seasonal occurrence probability of each spatial pattern of mean WEF and wind horizontal fields shown in Figure 5 and Figure 6.

ional component, between -240 and -40 (W/m), which is reflected in a slightly turned to the South dominant orientation (WSW).

Finally, the lowest values of WEF are observed in zones 9, 6 and 3, which are located at latitudes above the zone 8, in the East of the basin, and off the coastal zones of Colombia, Venezuela and Nicaragua (Figure 8). Time series of F_x and F_y in zone 9 show values between -650 and -250 (W/m) and between 20 and 140 (W/m), respectively (Figure 9). The latter depicts a predominant WNW-W orientation. Similarly, time series of zone 6, with values between -500 and -200 (W/m) and between -40 and 60 (W/m) for u and v , respectively (Figure9), show a dominant W-WNW orientation. As occurred in zones 5 and 4, components are also slightly turned southward in zone 3, with values between -400 and -150 (W/m) and between -80 and 0 (W/m) for u and v , respectively (Figure9), with a predominant W-WSW orientation.

4.5 Analysis of WEF direction at seasonal scale

Departing from time series of Figure 9 we study the direction of mean WEF at a seasonal scale for the 9 zones depicted in Figure 8. To obtain the annual cycle we compute the 60-year monthly mean for each zone and component (Figure 10).

Results illustrate a semi-seasonal signal in the zonal component of all regions characterized by two peaks. These peaks take place in January and June (see the most negative values), while the minimum values (in magnitude) are reached in April and September. These relative extremes are associated to the latitudinal migration of the ITCZ, which affects the magnitude of trade winds. Regarding the

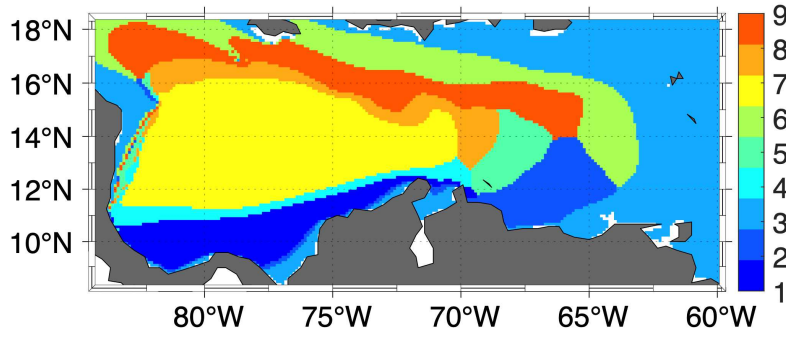


Fig. 8 Regions given by the temporal SOM analysis. SOM was applied with 3×3 neurons over the monthly mean WEF. We refer to these patterns in Figure and Figure 10.

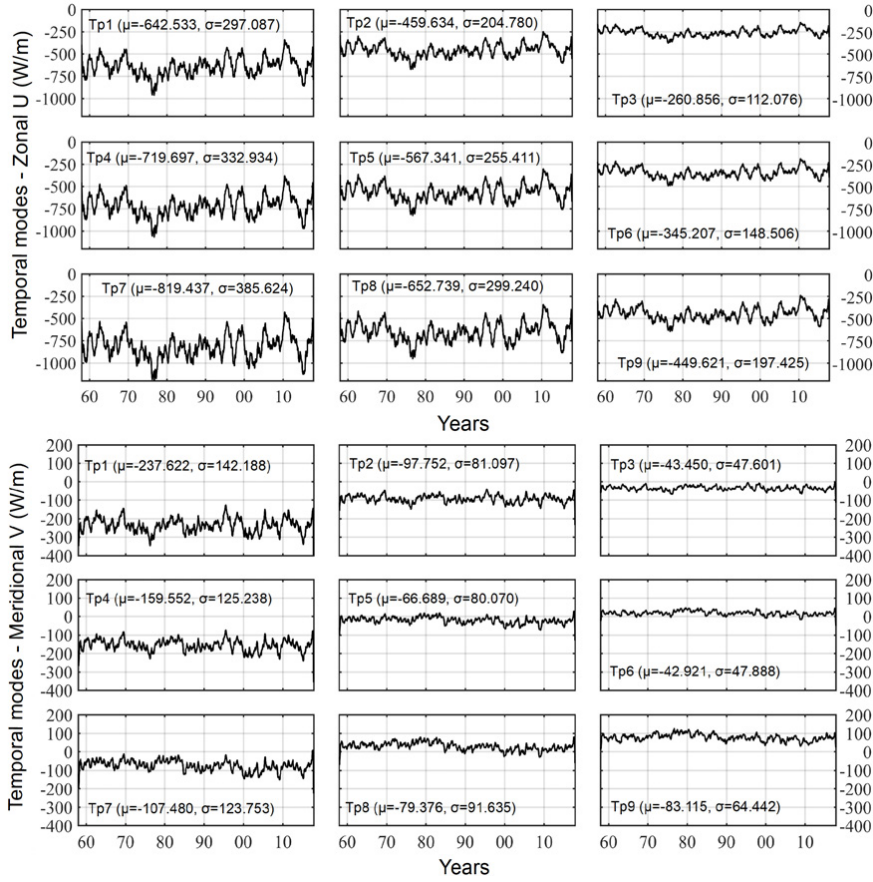


Fig. 9 Temporal patterns provided by a 3×3 SOM time domain analysis computed over the monthly mean WEF for zonal (F_x) and meridional (F_y) components (top and bottom panels, respectively). Names on the top-left side of every panel: Tp1, Tp2, ..., Tp9 refer to patterns shown in Figure 8. μ and σ are the mean and the standard deviation of every time series, respectively. Unit in W/m.

meridional component we find a mixed behavior: Zones 1, 2 and 4 also show two peaks (see Figure 10, bottom panel), while in northern regions such as 6, 8 and 9 there is only one peak, which takes place in May.

Figure 11 summarizes previous results showing the resultant 60-year monthly mean direction of WEF for every pattern shown in Fig. 8. As seen, the largest WEF (>1000 W/m) comes from east and east-northeast and correspond to patterns P7 and P4. Other modes such as P2, P3 and P9 represent weaker configurations (100-500 W/m), although waves keep coming from east-northeast or east-southeast, thus depicting small fluctuations in the direction throughout the year. This small variation in the direction is expected from dominant trade winds.

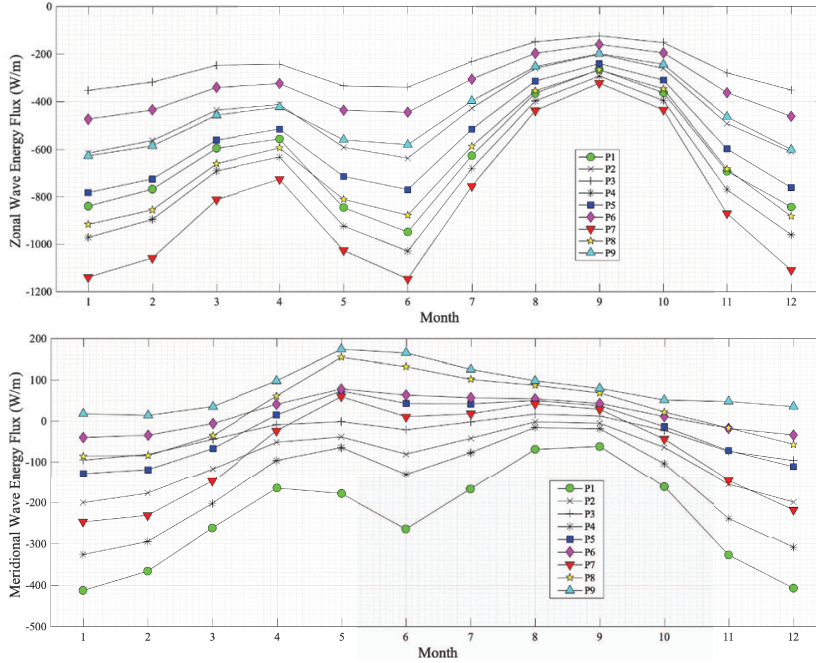


Fig. 10 60-year monthly mean WEF zonal (top panel) and meridional (bottom panel) components. Units in (W/m).

Figure 11 summarizes previous results showing the WEF roses at each region. The direction of the WEF ranges between the SW (P1, P2, P4 and P7) and NW (P8 and P9). The largest WEF is found in the areas corresponding to P1, P4 and P7.

4.6 Relationship between ENSO and the inter-annual variability of WEF

To evaluate the influence of ENSO on the inter-annual variability of WEF we have performed a correlation analysis between both variables. To this end, we use monthly time series of ONI and monthly mean WEF spanning from 1958 to 2017 (both included). Results show relatively large simultaneous correlations (of

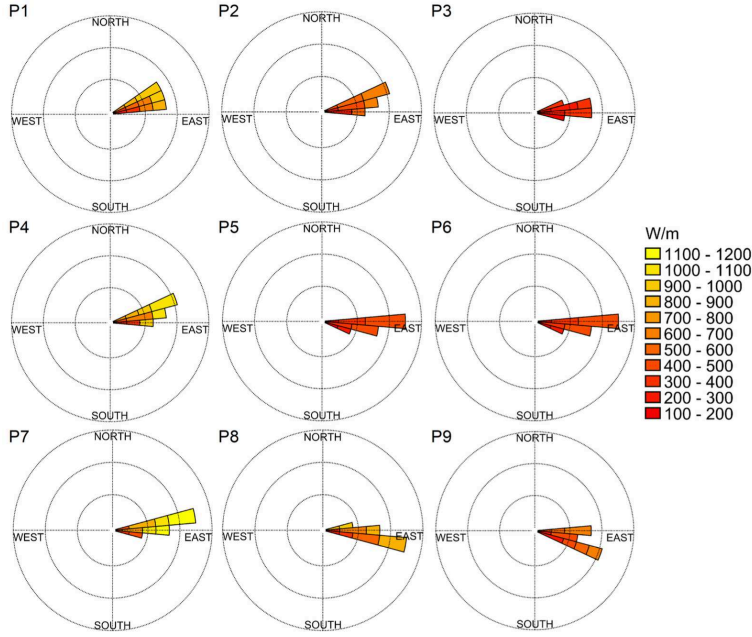


Fig. 11 Monthly mean WEF roses for the amplitudes shown in Figure 9, which correspond to the 9 zones displayed in Figure 8. Units in W/m.

about $r = 0.4$) between the mean WEF and the ONI off the Caribbean coasts of Colombia and in the central Caribbean Sea, at latitudes between 11°N and 17°N and longitudes between 70°W and 77°W (Figure 12). Lower positive correlations ($r \in [0.1, 0.2]$) are found at latitudes between 10°N and 17°N , and at longitudes between 77°W and 85°W . Conversely, negative correlations ($r \in [-0.3, -0.1]$) are observed off Venezuela coasts, in the southeastern Caribbean basin (Figure 12).

Next, we have computed the wavelet coherence (WTC) for all zones provided by the temporal SOM decomposition. Results shown that ENSO is correlated and coherent with the mean WEF over a long range of time scales and frequencies (Figure 13). The spectrum reveals a strong co-variability between ENSO and WEF in all regions for periods ranging from 24 to 32 months, and from 32 to 64 months. The longest period with significant correlations is 74 months (≥ 6 years). The relative phase indicates that ENSO leads WEF by 45° at periods between 32 and 64 months, and by 90° for periods between 64 and 72 months in all regions (see arrows in Figure 13 pointing downward). For example, for periods between 32 and 64 months WTC revealed a lag (ENSO leads) during 1993 and 1999 in all zones (see the large coherence during El Niño 1998). Moreover, there is a longer lag (ENSO leads) during 2001 and 2011 for regions 4–9. The WTC also reveals significant coherences between ENSO and mean WEF at a period between 24 and 40 months, as well as an increase in the coherence at a period between 24 and 92 months at the end of the two series, mainly in regions 1, 4 and 7 (Figure 13A-C, respectively). The coherence between 24 and 40 months is initially in-

phase for years 1964 and 1967, lagged (ENSO leads) between 1972 and 1974, and almost in-phase between years 1978 and 1983. Regarding the periods between 24 and 92 months, the coherence is lagged (ENSO leads) from 1993 to 2017. The larger positive correlation between WEF and ONI during El Niño events (either during Canonical or Modoki events, although is larger during Modoki) is likely caused by the strengthening of the CLLJ, especially in the Colombian basin [Wang, 2007, García-Martínez and Bollasina, 2020].

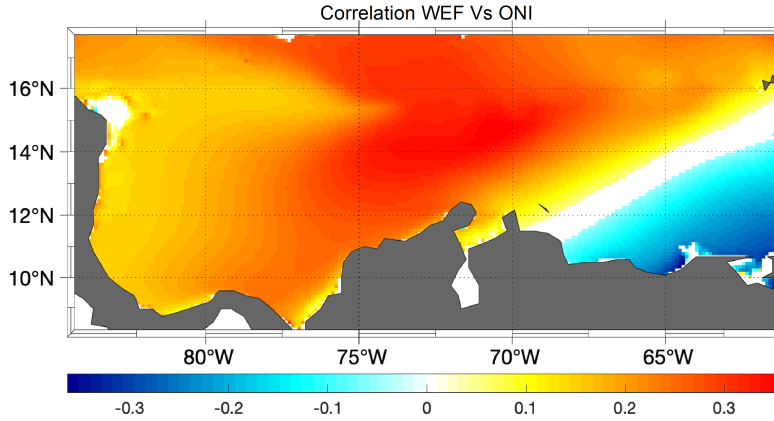


Fig. 12 Map of spatial correlation between monthly mean WEF and ONI for the study area. White color indicates a non statistically significant correlation. Red (blue) color indicate a positive (negative) correlation.

5 Discussion

Departing from a 60-year wave simulation we have analyzed the spatial and temporal variability of the mean wave energy flux (WEF). First, we have validated the simulated significant wave height (H_s) and mean wave period (T_{m-01}), against *in-situ* data from buoy 42058 of NOAA (Figure 2). Correlation, Weibull and Bias coefficients shown a good agreement between modeled and observed data. The database here used contributes to reduce the lack of available information on wave parameters in the Caribbean Sea [Orejarena-Rondón et al., 2021a]. Indeed this simulation is the longest in comparison to other wave reanalysis available in the Caribbean Sea [Arias et al., 2009, Dagua et al., 2013, Appendini et al., 2015, Osorio et al., 2016], and has been employed for marine energy analysis [Orejarena-Rondón et al., 2022], but can also be used for studies of coastal vulnerability, to analyze climate variability, or to study open sea extreme wave conditions for coastal and offshore engineering, among other. Data is freely accessible in the repository <https://nimbus.imedeo.uib-csic.es/s/JEaPEeeQNLPFJ3S> [Orejarena-Rondón et al., 2021b].

By applying a spatial SOM analysis over monthly mean WEF data we have regionalized WEF variability in the Caribbean Sea. Thus, wave information was classified into 9 patterns that collect the complex behavior of WEF (magnitude

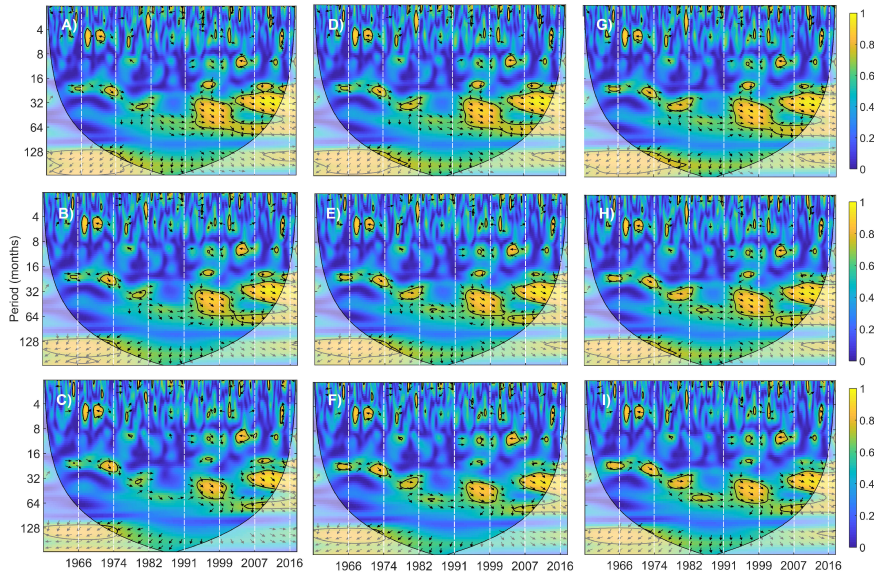


Fig. 13 Wavelet coherence (WTC) between monthly ONI and monthly mean WEF for all patterns provided by the temporal SOM analysis (Figure 8): (A) zone 1, (B) zone 2, (c) zone 3, (D) zone 4, (E) zone 5, (F) zone 6, (G) zone 7, (H) zone 8, and (I) zone 9. Arrows determine the phase between both series. Arrows pointing to the right represent positive correlation (in-phase signals). Arrows pointing to the left represent anti-correlation (anti-phase signals). Contours depict the wavelet squared coherence significant at 95%.

and direction). A similar analysis was also performed for surface horizontal wind. Results indicate that the behavior of mean WEF is strongly modulated by the seasonal variations of wind, which in turn changes with the latitudinal migration of the Inter Tropical Convergence Zone (ITCZ) over the Caribbean basin [Andrade, 1993, Andrade and Barton, 2013, Poveda et al., 2006]. The patterns (P_i) with more probability of occurrence are: P1 with 22.64% (dry season), the P6 with 17.36% (wet season) and the P7 with 14.58% (transition season), all of them associated with the growth in wave height and the change in wave period of waves as they move westward, reaching its maximum for P1 off the Colombian coasts. Other patterns are less frequent and distribute throughout the seasons: P4 and P2 occur during the dry season; P3 during the wet season (November); P5 and P8 occur in the transition season and at the beginning of the wet season. Finally, P9 occurs during both transition and wet seasons.

SOM analysis was also applied to surface winds used to force the model. Results are consistent with the 9 patterns obtained in the analysis of WEF (Figures 5 and 6 top panel). In this case, we observed the influence of the Caribbean Low Level Jet more toward the east between longitudes 68°W - 78°W and latitudes 11°N - 18°N , which differ from the influence zone of WEF (72°W - 83°W , and 10°N - 16°N). A plausible explanation is the large fetch in the Caribbean Sea, which allows wind waves some space to growth until they reach their most energetic state (Figures 5 and 6, top panels).

After that, we performed a temporal SOM analysis over the zonal and meridional component of WEF in the Caribbean Sea. As a result, we identified 9 zones of co-variability where WEF has different magnitudes and directions (Figures 7 and 8). Overall the zonal component is more energetic, due to the dominant trade winds. In particular, the most energetic zones are 7, 4, 1 and 8 (Figure 9 in the top panel). Regarding the meridional component, the most energetic zones are the 1, 4, 7 and 2. These results illustrate why the resultant direction is sometimes to the west (P1).

On the other hand, departing from above time series of WEF we have computed the seasonal cycle by calculating the 60-year monthly mean of zonal and meridional components, respectively. As a result, we get the seasonal cycle for each component and every region. Figure 10 illustrates the influence of ITCZ latitudinal displacements. Interestingly, the zonal component depicts a seasonal cycle with two peaks in all regions. However, the meridional component has one peak in the three regions located more to the north in the Caribbean Sea. The more energetic is the region the more clearly defined are the two peaks since the Caribbean Low-Level Jet, whose semi-annual cycle has been reported in previous works [Chunzai, 2007, Orfila et al., 2021], has a stronger influence. Unsurprisingly, the two peaks are more visible in the meridional component in those zones below 12°N (zones 1, 4 and 2). This is consistent with the description by [Andrade, 1993, Andrade and Barton, 2013, Poveda et al., 2006], who described that northernmost position of ITCZ is located between 10°N - 12°N . Above of this latitude the direction of WEF differs, as shown in Figure 11 for zones 6, 8 and 9.

Next, we have explored the relationship between ENSO and WEF at inter-annual scales. A correlation analysis show a strong positive correlation in the central part of the basin (0.4), lower but still positive in the Gulf of Darien (0.1–0.2), and negative off Venezuela (-0.3 to -0.1, Figure 12). This behavior is consistent with the findings of [Enfield and Mayer, 1997, Huang et al., 2002], who determined that when the Pacific warm anomalies during an ENSO event reach their maximum at the end of the year, trade winds weaken over the eastern Caribbean Sea at a latitude between 10°N and 20°N , and extend until Africa, while in the western Caribbean Sea trade winds strengthen.

Finally, to determine the periods and lag times of common variability between ENSO and WEF we compute the Wavelet Coherence (WTC). Results suggest the existence of a statistical between changes in ONI and WEF in different time periods, thus indicating that the monthly mean WEF is sensitive to changes in ENSO. All regions were correlated with the ONI for periods between 24 and 40 months during years 1964–1967, 1972–1974 and 1978–1983, characterized by the occurrence of large warm events in the eastern Pacific. This correlation occurs with the same phase in all periods, being larger between zones 4–9 (see Figure 13). Similarly, a strong correlation during years 1993–2017 is observed in all regions for a period that spans from 24 to 92 months, especially in zones 1, 4 and 7.

Acknowledgments

Authors acknowledge financial support from the Spanish Ministerio de Ciencia e Innovacion, Agencia Estatal de Investigación and FEDER through MOCCA Project (RTI2018-093941-B-C31). A. Orejarena-Rondon was supported by COL-

CIENCIAS (Call 727) and POGO-SCORE Visiting fellowship at the Mediterranean Institute for Advanced Studies. Authors acknowledge DIMAR (Dirección General Marítima from Colombia) for the wave parameters supplied for the model validation. J.M. Sayol thanks the joint funding received from the Generalitat Valenciana and the European Social Fund under grant APOSTD/2020/254.

References

- Alvarez-León et al., 1995. Alvarez-León, R., Aguilera-Quiñonez, J., Andrade, C., and Nowak, P. (1995). Caracterización general de la zona de surgencia en la guajira colombiana. *Boletín Academia Colombiana de Ciencias Exactas Físicas y Naturales*, 19:679–694.
- Amador, 1998. Amador, J. A. (1998). A climate feature of the tropical americas: the trade wind easterly jet. *Temas Meteorológicos y Oceanográficos*, 5(2):91–102.
- Andrade, 1993. Andrade, C. (1993). Análisis de la velocidad del viento en el mar caribe. *Boletín Científico CIOH*, pages 33–43.
- Andrade and Barton, 2013. Andrade, C. and Barton, E. (2013). Sobre la existencia de una celda atmosférica sobre el caribe y su efecto sobre las corrientes de Ekman en el mar caribe suroccidental. *Boletín Científico Centro de Investigaciones Oceanográficas e Hidrográficas, Cartagena, Colombia*, 31:73–94.
- Andrade et al., 2013. Andrade, C., Thomas, Y.-F., Alexandre, N.-L., Durand, P., and Anselme, B. (2013). Coastal flooding hazard related to swell events in Cartagena de Indias, Colombia. *Journal of Coastal Research*, 29:1126–1136.
- Appendini et al., 2015. Appendini, C. M., Urbano-Latorre, C. P., Figueroa, B., Dagua-Paz, C. J., Torres-Freyermuth, A., and Salles, P. (2015). Wave energy potential assessment in the Caribbean low level jet using wave hindcast information. *Applied Energy*, 137:375–384.
- Ardhuin and Orfila, 2018. Ardhuin, F. and Orfila, A. (2018). *Wind Waves*, chapter 14, pages 393–422. In *New Frontiers in Operational Oceanography*.
- Arias et al., 2009. Arias, A., Mesa, J., Bernal, G., and Montoya, M. (2009). Reconstrucción de cuarenta años de datos de oleaje en el mar caribe colombiano empleando el modelo wviiiTM y diferentes fuentes de datos. *Boletín Científico CIOH*, pages 37–56.
- Arinaga and Cheung, 2012. Arinaga, R. A. and Cheung, K. F. (2012). Atlas of global wave energy from 10 years of reanalysis and hindcast data. *Renewable Energy*, 39(1):49–64.
- Booij et al., 1999. Booij, N., Ris, R. C., and Holthuijsen, L. H. (1999). A third-generation wave model for coastal regions: 1. model description and validation. *Journal of Geophysical Research: Oceans*, 104(C4):7649–7666.
- Canals Silander and García Moreno, 2019. Canals Silander, M. F. and García Moreno, C. G. (2019). On the spatial distribution of the wave energy resource in Puerto Rico and the United States Virgin Islands. *Renewable Energy*, 136:442–451.
- Chunzai, 2007. Chunzai, W. (2007). Variability of the Caribbean low-level jet and its relations to climate. *Climate Dynamics*, 29(1):1432–1489.
- Cuttler et al., 2020. Cuttler, M. V., Hansen, J. E., and Lowe, R. J. (2020). Seasonal and interannual variability of the wave climate at a wave energy hotspot off the southwestern coast of Australia. *Renewable Energy*, 146:2337–2350.
- Dagua et al., 2013. Dagua, C., Lonin, S., Urbano, C., and Orfila, A. (2013). Calibración del modelo SWAN y validación de reanálisis del oleaje en el Caribe. *Boletín Científico CIOH*, 31:13–28.
- Dodet et al., 2010. Dodet, G., Bertin, X., and Taborda, R. (2010). Wave climate variability in the north-east Atlantic ocean over the last six decades. *Ocean Modelling*, 31(3):120–131.
- Elshinnawy et al., 2017. Elshinnawy, A. I., Medina, R., and González, M. (2017). On the relation between the direction of the wave energy flux and the orientation of equilibrium beaches. *Coastal Engineering*, 127:20–36.
- Enfield and Mayer, 1997. Enfield, D. B. and Mayer, D. A. (1997). Tropical Atlantic sea surface temperature variability and its relation to the Niño-Southern Oscillation. *Journal of Geophysical Research: Oceans*, 102(C1):929–945.
- Fiedler et al., 2015. Fiedler, J. W., Brodie, K. L., McNinch, J. E., and Guza, R. T. (2015). Observations of runup and energy flux on a low-slope beach with high-energy, long-period ocean swell. *Geophysical Research Letters*, 42(22):9933–9941.

- García-Martínez and Bollasina, 2020. García-Martínez, I. M. and Bollasina, M. A. (2020). Sub-monthly evolution of the caribbean low-level jet and its relationship with regional precipitation and atmospheric circulation. *Climate Dynamics*, 54(9):4423–4440.
- Grinsted et al., 2004. Grinsted, A., Moore, J., and Jevrejeva, S. (2004). Application of cross wavelet transform and wavelet coherence to geophysical time series. *Nonlinear Processes in Geophysics*, 11.
- Guillou, 2020. Guillou, N. (2020). Estimating wave energy flux from significant wave height and peak period. *Renewable Energy*, 155:1383–1393.
- Guillou et al., 2020. Guillou, N., Lavidas, G., and Chapalain, G. (2020). Wave energy resource assessment for exploitation—a review. *Journal of Marine Science and Engineering*, 8(9).
- Hanson et al., 2003. Hanson, H., Aarninkhof, S., Capobianco, M., Jiménez, J. A., Larson, M., Nicholls, R. J., Plant, N. G., Southgate, H. N., Steetzel, H. J., Stive, M. J. F., and de Vriend, H. J. (2003). Modelling of coastal evolution on yearly to decadal time scales. *Journal of Coastal Research*, 19(4):790–811.
- Hernández-Carrasco and Orfila, 2018. Hernández-Carrasco, I. and Orfila, A. (2018). The role of an intense front on the connectivity of the western mediterranean sea: The cartagena-tenes front. *Journal of Geophysical Research: Oceans*, 123(6):4398–4422.
- Huang et al., 2002. Huang, B., Schopf, P. S., and Pan, Z. (2002). The enso effect on the tropical atlantic variability: A regionally coupled model study. *Geophysical Research Letters*, 29(21):35–1–35–4.
- Iglesias et al., 2009. Iglesias, G., López, M., Carballo, R., Castro, A., Fraguera, J., and Frigaard, P. (2009). Wave energy potential in galicia (nw spain). *Renewable Energy*, 34(11):2323–2333.
- Japan Meteorological Agency, 2013. Japan Meteorological Agency, J. (2013). Research data archive at the national center for atmospheric research, computational and information systems laboratory. [urlhttps://doi.org/10.5065/D6HH6H41](https://doi.org/10.5065/D6HH6H41).
- Kobayashi et al., 2015. Kobayashi, S., Ota, Y., Harada, Y., Ebata, A., Moriya, M., Onoda, H., Onogi, K., Kamahori, H., Kobayashi, C., Endo, H., Miyaoka, K., and Takahashi, K. (2015). The jra-55 reanalysis: General specifications and basic characteristics. *Journal of the Meteorological Society of Japan*, 93:5–48.
- Kohonen, 1982. Kohonen, T. (1982). Self-organized formation of topologically correct feature maps. *Biological Cybernetics*, 43(3).
- Komen et al., 1984. Komen, G. J., Hasselmann, S., and Hasselmann, K. (1984). On the existence of a fully developed wind-sea spectrum. *Journal of Physical Oceanography*, 14(8):1271 – 1285.
- Liang et al., 2017. Liang, B., Shao, Z., Wu, G., Shao, M., and Sun, J. (2017). New equations of wave energy assessment accounting for the water depth. *Applied Energy*, 188:130–139.
- Liberti et al., 2013. Liberti, L., Carillo, A., and Sannino, G. (2013). Wave energy resource assessment in the mediterranean, the italian perspective. *Renewable Energy*, 50:938–949.
- Lin et al., 2019. Lin, Y., Dong, S., Wang, Z., and Guedes Soares, C. (2019). Wave energy assessment in the china adjacent seas on the basis of a 20-year swan simulation with unstructured grids. *Renewable Energy*, 136:275 – 295.
- Mentaschi et al., 2017. Mentaschi, L., Vousedoukas, M. I., Voukouvalas, E., Dosio, A., and Feyen, L. (2017). Global changes of extreme coastal wave energy fluxes triggered by intensified teleconnection patterns. *Geophysical Research Letters*, 44(5):2416–2426.
- Mirzaei et al., 2015. Mirzaei, A., Tangang, F., and Juneng, L. (2015). Wave energy potential assessment in the central and southern regions of the south china sea. *Renewable Energy*, 80:454–470.
- Nalley et al., 2016. Nalley, D., Adamowski, J., Khalil, B., and Biswas, A. (2016). Inter-annual to inter-decadal streamflow variability in quebec and ontario in relation to dominant large-scale climate indices. *Journal of Hydrology*, 536:426–446.
- Orejarena-Rondón et al., 2021a. Orejarena-Rondón, A. F., Orfila, A., Restrepo, J. C., Ramos, I. M., and Hernandez-Carrasco, I. (2021a). A 60 year wave hindcast dataset in the caribbean sea. *Data in Brief*, 37:107153.
- Orejarena-Rondón et al., 2021b. Orejarena-Rondón, A. F., Orfila, A., Restrepo, J. C., Ramos, I. M., and Hernandez-Carrasco, I. (2021b). A 60 year wave hindcast dataset in the southern caribbean sea. *Data in Brief*, page 107153.
- Orejarena-Rondón et al., 2022. Orejarena-Rondón, A. F., Restrepo, J. C., Correa-Metrio, A., and Orfila, A. (2022). Wave energy flux in the caribbean sea: Trends and variability. *Renewable Energy*, 181:616–629.

- Orfila et al., 2021. Orfila, A., Urbano-Latorre, C. P., Sayol, J. M., Gonzalez-Montes, S., Caceres-Euse, A., Hernández-Carrasco, I., and Muñoz, A. G. (2021). On the impact of the caribbean counter current in the guajira upwelling system. *Frontiers in Marine Science*, 8:128.
- Ortega et al., 2013. Ortega, S., Osorio, A. F., and Agudelo, P. (2013). Estimation of the wave power resource in the caribbean sea in areas with scarce instrumentation. case study: Isla fuerte, colombia. *Renewable Energy*, 57:240–248.
- Osorio et al., 2015. Osorio, A., Ortega Arango, S., and Arango-Aramburo, S. (2015). Assessment of the marine power potential in colombia. *Renewable and Sustainable Energy Reviews*, 56:966–977.
- Osorio et al., 2016. Osorio, A. F., Montoya, R. D., Ortiz, J. C., and Peláez, D. (2016). Construction of synthetic ocean wave series along the colombian caribbean coast: A wave climate analysis. *Applied Ocean Research*, 56:119–131.
- Ponce de León et al., 2016. Ponce de León, S., Orfila, A., and Simarro, G. (2016). Wave energy in the Balearic Sea. Evolution from a 29 year spectral wave hindcast. *Renewable Energy*, 85(C):1192–1200.
- Poveda, 2004. Poveda, G. (2004). La hidroclimatología de colombia: Una síntesis desde la escala inter-decadal hasta la escala diaria. *Rev. Acad. Colomb. Cienc*, 28:201–222.
- Poveda and Mesa, 1999. Poveda, G. and Mesa, O. (1999). La corriente de chorro superficial del oeste (“del chocÓ”) y otras dos corrientes de chorro atmosféricas sobre colombia: Climatología y variabilidad durante las fases del enso. *Revista de la Academia Colombiana de Ciencias Exactas Físicas y Naturales*, 23:517–528.
- Poveda et al., 2006. Poveda, G., Waylen, P. R., and Pulwarty, R. S. (2006). Annual and inter-annual variability of the present climate in northern south america and southern mesoamerica. *Palaeogeography, Palaeoclimatology, Palaeoecology*, 234(1):3–27. Late Quaternary climates of tropical America and adjacent seas.
- Reguero et al., 2015. Reguero, B., Losada, I., and Méndez, F. (2015). A global wave power resource and its seasonal, interannual and long-term variability. *Applied Energy*, 148:366–380.
- Reguero et al., 2019. Reguero, B., Losada, I., and Méndez, F. (2019). A recent increase in global wave power as a consequence of oceanic warming. *Nature Communications*, 10.
- Restrepo et al., 2019. Restrepo, J. C., Higgins, A., Escobar, J., Ospino, S., and Hoyos, N. (2019). Contribution of low-frequency climatic–oceanic oscillations to streamflow variability in small, coastal rivers of the sierra nevada de santa marta (colombia). *Hydrology and Earth System Sciences*, 23(5):2379–2400.
- Rivera-Páez and Molares, 2003. Rivera-Páez, S. and Molares, R. (2003). Evidencias de la oscilación del tiempo madden y julian en el caribe colombiano. *Boletín Científico CIOH*, pages 101–113.
- Teuvo, 1997. Teuvo, K. (1997). Exploration of very large databases by self-organizing maps. In *Proceedings of International Conference on Neural Networks (ICNN’97)*, volume 1, pages PL1–PL6 vol.1.
- Wang, 2007. Wang, C. (2007). Variability of the caribbean low-level jet and its relations to climate. *Climate Dynamics*, 29(4):411–422.
- Waters et al., 2009. Waters, R., Engström, J., Isberg, J., and Leijon, M. (2009). Wave climate off the swedish west coast. *Renewable Energy*, 34(6):1600–1606.
- Wiggins et al., 2019. Wiggins, M., Scott, T., Masselink, G., Russell, P., and McCarroll, R. J. (2019). Coastal embayment rotation: Response to extreme events and climate control, using full embayment surveys. *Geomorphology*, 327:385–403.
- Wu et al., 2017. Wu, L., Qin, J., Wu, T., and Li, X. (2017). Trends in global ocean surface wave characteristics as represented in the era-interim wave reanalysis for 1979–2010. *Journal of Marine Science and Technology*, 23.